In Situ Cloud Sensing with Multiple Scattering Lidar: Simulations and Demonstration

K. FRANKLIN EVANS
Program in Atmospheric and Oceanic Sciences, University of Colorado, Boulder, Colorado

R. PAUL LAWSON, PAT ZMARZLY, AND DARREN O'CONNOR
SPEC Inc., Boulder, Colorado

WARREN J. WISCOMBE
NASA Goddard Space Flight Center, Greenbelt, Maryland

(Manuscript received 24 February 2003, in final form 2 May 2003)

ABSTRACT

Due to the spatially inhomogeneous nature of clouds there are large uncertainties in validating remote sensing retrievals of cloud properties with traditional in situ cloud probes, which have sampling volumes measured in liters. This paper introduces a new technique called in situ cloud lidar, which can measure extinction in liquid clouds with sampling volumes of millions of cubic meters. In this technique a laser sends out pulses of light horizontally from an aircraft inside an optically thick cloud, and wide-field-of-view detectors viewing upward and downward measure the time series of the number of photons returned. Diffusion theory calculations indicate that the expected in situ lidar time series depends on the extinction and has a functional form of a power law times an exponential, with the exponential scale depending on the distance to the cloud boundary. Simulations of 532-nm wavelength in situ lidar time series are made with a Monte Carlo radiative transfer model in stochastically generated inhomogeneous stratocumulus clouds. Retrieval simulations are performed using a neural network trained on three parameters fit to the time series of each detector to predict 1) the extinction at four volume-averaging scales, 2) the cloud geometric thickness, and 3) the optical depth at four averaging scales. Even with an assumed 20% lidar calibration error the rms extinction and optical depth retrieval accuracy is only 12%. Simulations with a dual wavelength lidar (532 and 1550 nm) give accurate retrievals of liquid water content and effective radius. The results of a mountain-top demonstration of the in situ lidar technique show the expected power-law time series behavior.

1. Introduction

Understanding and predicting the radiative impacts of clouds on the earth's climate is complicated by the large variability of cloud microphysical properties, both across different cloud types and within even a single cloud. Traditionally, in situ measurements of cloud optical properties have been carried out with optical particle counting probes that attempt to measure droplet size distributions [e.g., the Particle Measuring Systems Forward Scattering Spectrometer Probe (FSSP) and 2D imaging probes, Knollenberg 1981]. Light scattering calculations (e.g., Mie theory for spherical droplets) are then applied to the size distributions to estimate the desired optical properties, such as volume extinction, single scattering albedo, and asymmetry parameter. More recently, as in situ measurements have been sought for cloud-radiation studies, cloud probes have been designed to directly measure optical properties, such as an airborne transmissometer (Korolev et al. 1999), a cloud extinctometer (Zmarzly and Lawson 2000), and a cloud integrating nephelometer (Gerber et al. 2000).

A common problem with in situ cloud measurements, whether of microphysical or optical properties, is their small sampling volumes. The FSSP-100, for example, measures a volume of about 300 cm^3 in a 1-km traverse. Considering that a cumulus cloud can contain 10^{15} cm^3, the FSSP samples a tiny fraction of the cloud volume. This is significant because of the extreme variability of cloud density down to centimeter scales (Baker 1992; Davis et al. 1999b). The sampling volumes of traditional cloud probes are totally inadequate to characterize the bulk properties of clouds.

Remote sensing methods observe large cloud volumes, but the measurements tend to be more indirectly related to cloud properties. For example, visible/near-infrared solar reflectance techniques (e.g., Nakajima and King 1990) retrieve cloud optical depth and effective

---

Corresponding author address: Dr. K. Franklin Evans, University of Colorado, 311 UCB, Boulder, CO 80309-0311.
E-mail: evans@nit.colorado.edu

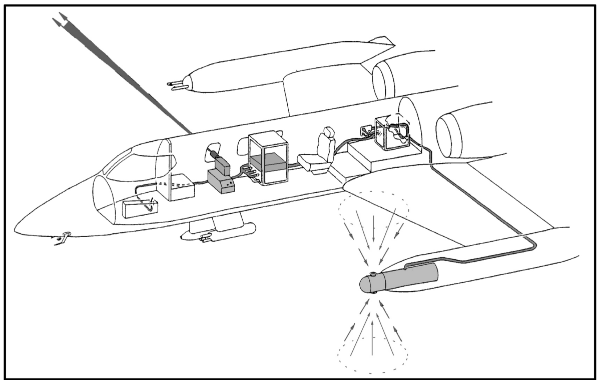

FIG. 1. An artist's rendition of the in situ cloud lidar, showing the laser beam exiting the Learjet cabin window to the right, while upward- and downward-viewing detectors on the left wingtip record a time series of the multiply scattered light.

radius, but the effective radius is weighted toward the cloud top (e.g., Platnick 2000) and the errors from three-dimensional radiative transfer effects are substantial (Varnai and Marshak 2001). Active remote sensing techniques such as cloud radar can retrieve range-resolved cloud properties (Liao and Sassen 1994; Fox and Illingworth 1997; Donovan and van Lammeren 2001). Since cloud radars measure the sixth moment of the droplet size distribution, these measurements are also rather indirectly related to the desired quantities, such as liquid water content (proportional to the third moment) and visible extinction (proportional to the second moment). In situ cloud measurements generally have the advantage of being more directly related to the desired microphysical or optical properties than remote sensing measurements.

An important application of in situ cloud measurements is validation of cloud remote sensing measurements. Comparisons of in situ and remote sensing measurements are hampered by the mismatch in sampling volumes. Given the observed variability inside clouds (e.g., Davis et al. 1999b), the sampling error from extrapolation of the in situ cloud probe measurement of a few liters to the remote sensing measurement of millions of cubic meters is probably as large as the expected retrieval error. Thus, an accurate in situ cloud measurement technique that could sample a volume of millions of cubic meters would be very valuable for validating active and passive cloud remote sensing techniques.

This paper describes a new cloud measurement technique we call in situ lidar. The in situ lidar differs from a regular lidar in that it uses a very wide field-of-view detector pointed away from the laser beam direction (see Fig. 1 for a depiction of a proposed instrument). Inside an optically thick cloud the laser pulse is multiply scattered by cloud droplets and a small portion of the light returns to be measured by the detectors. The signal measured by the instrument is the number of photons returned as a function of time. The amplitude and shape of the returned pulse contain information about the distance to the cloud boundaries and the volume average extinction (units of km^{-1}) in water clouds at different spatial scales around the instrument. The in situ cloud lidar thus works by taking advantage of the multiple scattering, rather than avoiding it as is done in conventional lidar research. This in situ cloud lidar concept was inspired by an omnidirectional multiple scattering lidar technique used to characterize the scattering and absorption coefficient in Antarctic ice (Askebjer et al. 1997). In addition to its obvious application for validating cloud remote sensing, we believe that the in situ lidar will be valuable for cloud physics and chemistry research by providing measurements of water droplet surface area (proportional to extinction) that are more representative of cloud average values than those from current in situ techniques.

The most similar passive in situ sensing instrument is the cloud absorption radiometer (King 1986), which retrieves the single scattering albedo at a number of wavelengths from the angular characteristics of the diffusing solar radiation deep inside a cloud. Multiple scattering based lidar cloud remote sensing techniques have been developing recently. The method of Bissonnette and Hutt (1995) retrieves extinction and effective particle diameter profiles in clouds with optical depths up to about 4 using a traditional lidar setup. For optically thick clouds the ''off-beam'' lidar technique has been proposed to remotely sense both optical depth and geometric thickness of a cloud layer (Davis et al. 1999a). A ground-based wide angle imaging lidar (Love et al. 2001) built at Los Alamos National Laboratory has operated with a YAG 532-nm laser and a special-purpose high-speed photon-counting imager. An aircraft-based instrument, Thickness from Off-beam Returns (THOR), built at National Aeronautics and Space Administration (NASA) Goddard Space Flight Center, successfully operated on its first test flight in March 2002. Both the off-beam lidar technique and the in situ lidar technique take advantage of multiple scattering and photon diffusion to retrieve properties over large cloud volumes.

SPEC, Inc., built and operated a prototype in situ cloud lidar in spring 2002. The prototype lidar consisted of a vertically pointing Nd:YAG laser operating at a wavelength of 532 nm and a detector based on a photomultiplier tube. In April 2002 the lidar was deployed on a mountaintop at the Storm Peak Laboratory above Steamboat Springs, Colorado. This brief experiment successfully demonstrated the in situ cloud lidar concept. NASA has funded SPEC with a 2-yr Small Business Innovative Research contract to develop a prototype airborne instrument.

The next section of the paper discusses how diffusion theory can be used to understand the in situ lidar technique. Section 3 reports on simulations of a 532-nm wavelength in situ lidar in inhomogeneous stratocumulus clouds, an inversion technique for volume-averaged extinction, cloud thickness, and optical depth, and estimates of the retrieval accuracy. Section 4 describes the prototype in situ cloud lidar built by SPEC, Inc. and some results of the test of this prototype. Section 5 explores the potential of expanding the concept to a two-wavelength lidar for measuring liquid water content and effective radius. Section 6 summarizes the results and describes plans for building a prototype airborne in situ lidar.

2. Diffusion theory for the in situ lidar

In an optically dense cloud the photons in the lidar pulse are scattered before propagating very far. The mean distance between scattering events is $1/\beta$, where β is the volume extinction coefficient. This ‘‘mean free path’’ is typically 10–100 m. The photons scatter many times because there is virtually no absorption at the 532-nm wavelength and the cloud is optically thick. Since the cloud droplets are large compared to the laser wavelength, most of the time the photons scatter by a small angle. However, there are so many scattering events that the photons eventually travel in all directions and spread out of the laser beam to cover the region around the lidar with a diffuse light. At this point the photon behavior may be described as a random walk and diffusion theory may be applied. The photons diffuse away in all directions from the lidar source and eventually leak out of the cloud.

Given the tremendous number of photons emitted by the laser, some will find their way back to the detectors. If a detector is pointed in the direction of the lidar beam, then many photons will return quickly by backscattering. For a detector pointed away from the lidar beam, the paths to the detector are more circuitous, fewer photons will be detected, and they will typically take longer to arrive. The larger the cloud extinction, the more photons will scatter into the detector and the longer it will take for the swarm of photons to diffuse away. If there is a small amount of absorption, that absorption is made detectable by the large number of scattering events a photon undergoes. As the lidar pulse spreads and diffuses throughout the cloud, the boundaries of the cloud are felt. The number of photons detected decreases more rapidly once the diffusion bubble reaches the cloud boundary.

A diffusion solution to the radiative transfer equation can approximate the in situ lidar situation. This problem is similar to that of lightning radiative transfer in clouds, which has been treated with diffusion theory by Koshak et al. (1994). The notation used here follows Davis and Marshak (2002) who use diffusion theory for the cloud transmission problem. Diffusion theory is appropriate after the lidar pulse photons have scattered enough times that all knowledge of their initial direction is lost. The time to reach the diffusion regime (t_d) is roughly twice the time to cover a transport mean free path (l_t):

$$t_d \approx \frac{2l_t}{c} = \frac{2}{c(1 - \omega_0 g)\beta}, \tag{1}$$

where $l_t = 1/[(1 - \omega_0 g)\beta]$, c is the speed of light, ω_0 is the single scattering albedo, and g is the asymmetry parameter. For wavelengths shorter than about 0.9 μm there is essentially no absorption, so $\omega_0 = 1$. For typical liquid cloud droplet distributions $g = 0.84 - 0.87$ is derived from Mie theory. The transport mean free path corrects the mean free path for the predominance of forward scattering.

The key radiative quantity in diffusion theory is the scalar flux, J. The scalar (or actinic) flux is related to the mean radiance $\bar{I}$ by $J = 4\pi\bar{I}$ and to the radiant energy density U by $J = cU$. In a homogeneous medium the diffusion equation for the scalar flux is (Davis and Marshak 2002)

$$\frac{\partial J}{\partial t} - D\nabla^2 J = -c\beta_a J, \tag{2}$$

where D is the diffusion coefficient with units of squared meters per second and $\beta_a = (1 - \omega_0)\beta$ is the absorption coefficient. In a homogeneous medium the diffusion coefficient is

$$D = \frac{cl_t}{3} = \frac{c}{3(1 - \omega_0 g)\beta}. \tag{3}$$

The diffusion equation can be solved by Fourier transforming the equation in space, solving the first-order ordinary differential equation in time, and transforming back. The radiance in direction $\mathbf{\Omega}$ may then be obtained from the scalar flux by $I(t, \mathbf{r}, \mathbf{\Omega}) = (1/4\pi)[1 - l_t\mathbf{\Omega} \cdot \mathbf{\nabla}]J(t, \mathbf{r})$.

The solution to the diffusion equation for an isotropic, instantaneous pulse of light emitted from a infinitesimal source at the origin is

$$J(t, r) = \frac{E_p c}{(4\pi D t)^{3/2}} e^{-c\beta_a t} \exp\left(-\frac{r^2}{4Dt}\right), \tag{4}$$

where E_p is the energy in the emitted pulse. The solution is a Gaussian in radius r whose width is proportional to the square root of time:

$$\langle r^2 \rangle^{1/2} = \sqrt{2Dt} = \sqrt{\frac{2ct}{3(1 - \omega_0 g)\beta}}. \tag{5}$$

An extinction of 60 km^{-1} gives a diffusion timescale of 0.8 μs, which corresponds to an rms radius of about 140 m. Of course, a highly directed lidar pulse is not isotropic, but it becomes effectively isotropic after traveling about one transport mean free path. For arrival times in the diffusion regime, a detector collocated with the lidar is close to the maximum of the Gaussian scalar flux field where the radiance field is isotropic. The radiance is obtained from (4) with $r = 0$, giving

$$I \approx \frac{E_p c}{(4\pi)^{5/2}(Dt)^{3/2}} e^{-c\beta_a t}. \tag{6}$$

The energy received by a detector is $E_d = IA_d\Omega_d\Delta t$ where A_d is the detector area, Ω_d is the detector solid angle, and Δt is the detector time bin size. In this paper the detected energy is expressed by the fraction of emitted photons per detector area per detector solid angle per time. In the diffusion regime in a uniform infinite cloud the photon fraction is then

$$f_p = \frac{E_d}{E_p A_d \Omega_d \Delta t} = \frac{c}{(4\pi)^{5/2}} \left[\frac{3(1 - \omega_0 g)\beta}{ct}\right]^{3/2} e^{-c\beta_a t}. \quad (7)$$

This equation shows the relationship between the measured time series signal and the extinction β. It is actually the scaled extinction $(1 - \omega_0 g)\beta$ that is measured, but the scaled extinction is precisely the quantity that is most important radiatively. In liquid clouds the asymmetry parameter g is well known, allowing the actual extinction to be readily determined. For a homogeneous infinite cloud, diffusion theory predicts that the in situ lidar signal is a power law in time multiplied by an exponential if there is absorption.

The diffusion equation also can be solved for a homogeneous medium with boundaries in the vertical. The boundary condition is no flux entering at cloud base and top. These boundary conditions translate to a linear constraint on the scalar flux J and its derivative $\partial J/\partial z$. It is simpler to use the linear extrapolation approximation (e.g., see Koshak et al. 1994) and set the scalar flux to zero somewhat beyond the actual boundaries, $J(z = H/2 + 2l_t/3) = 0$ and $J(z = -H/2 - 2l_t/3) = 0$, where H is the cloud thickness and $(2/3)l_t$ is the extrapolation length, which is usually small compared to the cloud thickness. The solution method is to apply a Fourier transform to the diffusion equation in x and y, but use a Fourier cosine series in z with each term satisfying the boundary conditions. The solution for an isotropic pulse of light emitted at the origin is

$$J(t, r) = \frac{E_p c}{4\pi D t} e^{-c\beta_a t} \exp\left(-\frac{x^2 + y^2}{4Dt}\right) \times \sum_{n=1,3,\ldots}^{\infty} \frac{2}{H_e} e^{-Dt\gamma_n^2} \cos(\gamma_n z) \qquad \gamma_n = \frac{\pi n}{H_e}, \quad (8)$$

where $H_e = H + (4/3)l_t$ is the cloud thickness including the extrapolation lengths. For times in which the radius of the photon bubble is small compared to the distance to the boundaries, the Fourier sum over odd terms is a Gaussian function and the scalar flux agrees with the diffusion solution for the infinite medium. The scalar flux is again evaluated at the origin and converted to photon fraction to give the in situ lidar time series

$$f_p = \frac{c}{(4\pi)^2 D t} \frac{2}{H_e} e^{-c\beta_a t} \sum_{n=1,3,\ldots}^{\infty} e^{-Dt\gamma_n^2}. \quad (9)$$

For times $t > H_e^2/(20D)$ (e.g., $t > 3.8$ μs for $\beta = 60$ km^{-1}, $\omega_0 = 1$, $g = 0.86$, and $H = 800$ m) the sum is dominated by the first term. Thus for a nonabsorbing uniform medium, diffusion theory predicts that the time series behavior at later times is a power law (t^{-1}) multiplied by an exponential (e^{-t/t_b}) with the timescale $t_b = 3H_e^2/(\pi^2 c l_t)$. The photon fraction for times $t < H_e^2/(20D)$ is well approximated by the infinite medium solution, which is simply a power law ($t^{-3/2}$) for nonabsorbing media.

A comparison was made between the diffusion model and the Monte Carlo model described in the next section for a uniform water cloud with thickness $H = 800$ m, extinction $\beta = 60$ km^{-1}, and asymmetry parameter $g = 0.86$ (from Mie theory for effective radius $r_e = 8$ μm at 532 nm). After about 2 μs the diffusion model time series has the same shape as the Monte Carlo result but is higher by a factor of about 1.3. We ascribe this to the directed laser beam and forward scattering medium, which cause the photon bubble to be offset from the lidar and elongated in the direction of the beam instead of symmetric around the detector as assumed by the diffusion model. An experiment with an equivalent isotropic scattering medium showed agreement between the diffusion and Monte Carlo models to within 10% throughout the whole time series.

3. In situ lidar retrieval simulations

a. Monte Carlo radiative transfer model

The modeling results shown in this article are generated with a special-purpose forward Monte Carlo model. The model simulates many photon trajectories from the laser to the detectors. At each scattering event the photon is scattered to a new direction according to the Mie phase function in that grid box. The photon travel time is simply the total photon distance traveled to the detector divided by the speed of light. A photon trajectory is ended when its travel time exceeds a specified maximum time.

Since it is very unlikely for a photon to travel into a detector, instead at each scattering event the probability for a photon to travel directly to the detector is determined (if the event is in the detector field of view). This probability is added to the detector signal for the appropriate time bin. The probability to scatter into a detector is

$$p_d = \mathcal{T}(\mathbf{x}, \mathbf{x}_d) P(\mathbf{\Omega} \cdot \mathbf{\Omega}')(-\mathbf{n} \cdot \mathbf{\Omega} A_d/R^2), \quad (10)$$

where $\mathcal{T}(\mathbf{x}, \mathbf{x}_d)$ is the transmission from the scattering event location ($\mathbf{x}$) to the detector location ($\mathbf{x}_d$), and $P(\mathbf{\Omega} \cdot \mathbf{\Omega}')$ is the phase function for scattering from the photon incident direction $\mathbf{\Omega}'$ to the direction to the detector $\mathbf{\Omega}$. The term $-\mathbf{n} \cdot \mathbf{\Omega} A_d/R^2$ is the projected solid angle of the detector, where A_d is the area of the detector, $\mathbf{n}$ is the unit normal vector in the direction the detector views, and R is the distance from the scattering event to the detector. The statistical Monte Carlo noise is large when only a few of the many simulated photons make a large contribution to the lidar signal. All three factors in the probability of the photon traveling to the detector are sources of Monte Carlo noise. Most of the photons are too far from the detector to have a significant transmission. If a scattering event is very close to the detector (R small), then the detector solid angle can be very large, and if a photon is initially heading nearly straight toward the detector, then the phase function, with its very strong forward peak, will be huge.

A reduction in the latter two sources of Monte Carlo noise is made by pretending that there is a much larger *virtual* detector. Once the signal is in the diffusion regime, it should not change if the detector is moved by a distance that is small compared to a mean free path. The probability to scatter to the detector is integrated over the large area of the virtual detector, which smooths over the narrow forward peak in the phase function. The lidar signal for the virtual detector is then scaled to that of the actual detector by the ratio of the detector areas. The integral of the phase function over the solid angle of the virtual detector is precalculated and stored in a lookup table. The radius of the virtual detector disk is the smaller of 0.2 times the local mean free path and 10% of the total photon distance, which simulations show is small enough so that the results are not affected significantly by the use of the virtual detector. The virtual detector approach reduces the Monte Carlo noise by more than an order of magnitude.

The optical properties (extinction, single scattering albedo, and phase function) are specified on a three-dimensional grid input to the Monte Carlo model. The optical properties are assumed to be uniform in each grid cell. The surface has uniform Lambertian reflection specified by the albedo. The laser beam has a Gaussian profile specified by a half-width at half-maximum. Multiple detectors, with arbitrary pointing directions and uniform sensitivity inside the field of view, can be simulated. The lidar signal can be output either for linear or logarithmic spaced time bins. An estimate of the Monte Carlo noise at each time sample is generated from the variance over 25 batches of photons. The lidar signal output is the photon fraction in units of $(\mu\text{s ster cm}^2)^{-1}$.

b. Stratocumulus stochastic cloud generation

Fractal models are often used to simulate turbulently mixed clouds because they can capture the observed statistics and generate fields more rapidly and with a larger range of scales than large eddy simulation models. There are two common methods for generating fractal clouds: cascades, such as the bounded cascade (Cahalan et al. 1994), and Fourier filtering methods (Schertzer and Lovejoy 1987; Barker and Davies 1992). Here the Fourier filtering approach is used to generate overcast liquid cloud fields with variability in all three dimensions. Two correlated stochastic fields are generated: liquid water content (LWC) and droplet number concentration (N).

The procedure starts by generating independent Gaussian random numbers for the Fourier components of one three-dimensional field. The Gaussian random deviates for the second field are generated with a specified correlation to the first field. The two Fourier noise fields are filtered with a power law in the wavenumber (k^α) specified by a slope parameter α. This has the effect of reducing the power in the high spatial frequencies, thus introducing spatial correlations. Using a power law as the Fourier filter results in scaling or fractal behavior of the cloud field. The two real filtered Gaussian noise fields are then Fourier transformed, which can be performed with one complex FFT. The resulting fields are periodic, which is desired in the horizontal but not in the vertical. Therefore, only half of the vertical levels in the generated fields are used further. Since cloud LWC is observed to resemble a lognormal distribution, the first transformed field is scaled to achieve the specified log standard deviation, and then exponentiated. Actual clouds do not have mean LWC profiles that are uniform with height. For stratocumulus the mean LWC profile is observed to increase linearly with height throughout most of the layer following the adiabatic LWC profile. Near the top of the cloud layer the mean LWC profile decreases rapidly due to entrainment of dry air above the temperature inversion. This behavior is simulated by multiplying the stochastic LWC field by a piecewise linear profile consisting of two segments, which are zero at the cloud bottom and top for these clouds. After this profile modulation, the LWC field is scaled to obtain the desired mean liquid water path (LWP).

The second stochastic Gaussian field is used for the droplet concentration field, and is simply scaled and shifted to give the specified mean and standard deviation of number concentration. The LWC and number concentration at each point in the field are combined to obtain the effective radius assuming a gamma droplet size distribution with an effective variance of 0.1. This stochastic cloud model for stratocumulus clouds is specified by eight parameters: mean liquid water path, standard deviation of log of LWC (before profile is applied), Fourier space power-law spectral slope, Gaussian correlation between LWC and N, mean and standard deviation of droplet concentration (N), fractional altitude of maximum of LWC, and cloud layer thickness. There are also other auxiliary parameters such as the horizontal domain size and the grid spacing.

For the in situ lidar modeling 100 cloud fields are simulated. Six of the eight stochastic cloud field parameters, including the cloud thickness and amount of variability, are themselves chosen randomly from a uniform distribution. The cloud mean liquid water path is obtained indirectly by randomly choosing the mean value of the increase in LWC with height (with units of g m^{-2} km^{-1}), so that the LWP is proportional to the cloud thickness squared. In addition, the cloud-base height and surface albedo are randomly selected for each field. Table 1 lists the ranges of parameter used in the simulation. The horizontal domain is 3.2 km × 3.2 km with 25-m grid spacing (128 × 128 grid). Figure 2 shows a Y–Z cross section of liquid water content and effective radius in one of the stochastic cloud fields (labeled StCu21).

TABLE 1. Stochastic cloud field parameters for the stratocumulus (stCu) modeling.*

Parameter	Range	StCu21	StCu6
Cloud thickness (km)	0.20–1.00	0.825	0.425
Mean LWC km^{-1} (g m^3 km^{-1})	0.5–1.5	1.03	0.91
Std dev log LWC (before profile modulation)	0.1–0.8	0.17	0.79
Spectral power-law slope	−1.5–−2.0	−1.92	−1.66
Correlation between LWC and concentration	0.75	0.75	0.75
Mean droplet concentration (cm^{-3})	50–300	177	198
Std dev of concentration	Mean/4	44	49
Fractional height of modulation profile	0.9	0.9	0.9
Cloud-base height (km)	0.3–0.6	0.427	0.334
Surface albedo	0.05–0.25	0.110	0.067

* When a range in parameter values is given, a uniform distribution between these values is used.

This is one of the thicker, smoother, and least variable fields (see parameters listed in Table 1). The procedure of using two stochastic fields to specify the LWC and droplet concentration fields separately results in more realism in the relationship between effective radius and LWC (Fig. 3). A typical parameterization would give a single effective radius for each LWC, rather than the more appropriate spread of values. The goal with these parameter choices is to cover a wide range of variability to represent all stratocumulus clouds.

With the gamma droplet size distribution assumption, the cloud physical properties of liquid water content and effective radius are converted to optical properties of volume extinction, single scattering albedo, and phase function using Mie theory at the 532-nm laser wavelength. Since water droplets do not absorb at 532 nm, the single scattering albedo is equal to unity. The phase function is weakly dependent on the effective radius. Thus extinction is the key optical property of clouds that is variable for visible wavelengths. Figures 4 and 5 show *Y–Z* cross sections of extinction and the vertical integral of extinction (optical depth) for two fields. Compared to the StCu21 field, the StCu6 field has smaller cloud thickness, more variability (larger standard deviation of the log LWC), and greater roughness (less steep Fourier spectral slope).

c. *In situ lidar simulations*

The forward Monte Carlo model is used to simulate in situ lidar time series at four positions in each of the 100 stochastic cloud fields. The positions are 0.4, 1.2, 2.0, and 2.8 km in *Y* and 1.6 km in *X*. The lidar altitude is randomly chosen between 10% and 90% of the cloud depth. The lidar geometry is as depicted in Fig. 1. The laser is pointed in the $+X$ direction (along the airplane wing) and has a Gaussian beamwidth of 2° (half-width at half-maximum). Two detectors located 8 m in the $-X$ direction from the laser are simulated pointing in the

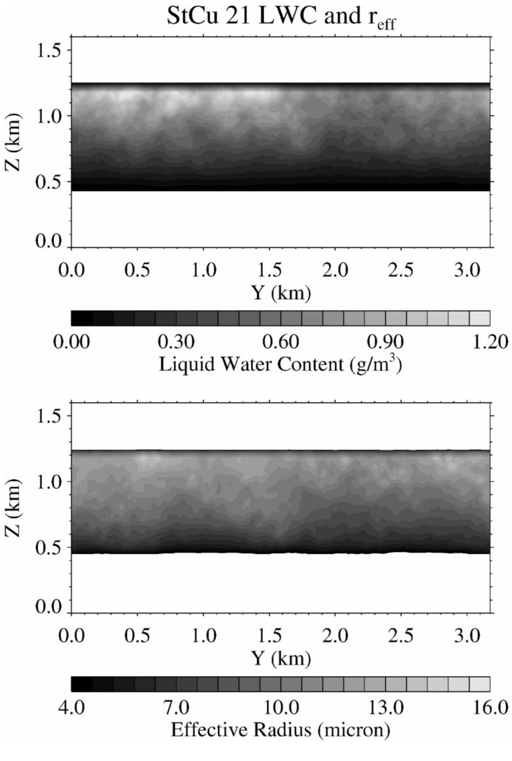

FIG. 2. An *Y–Z* cross section of liquid water content and effective radius in the simulated cloud field labeled StCu21.

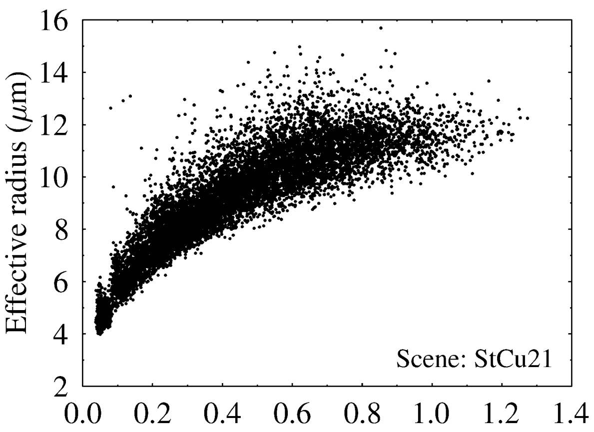

FIG. 3. Scatterplot of effective radius vs liquid water content in cloud field StCu21.

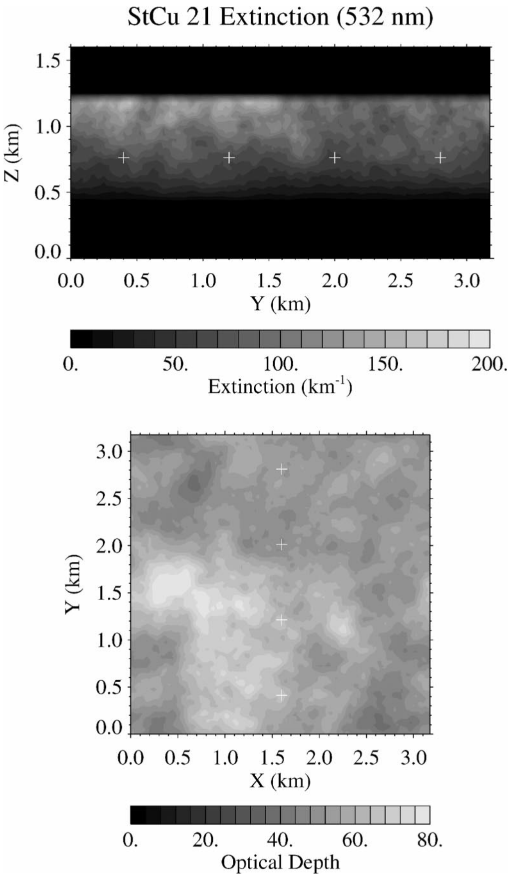

FIG. 4. An Y–Z cross section of extinction and X–Y plot of optical depth for stochastic cloud field StCu21. The crosses show locations where the in situ lidar was simulated.

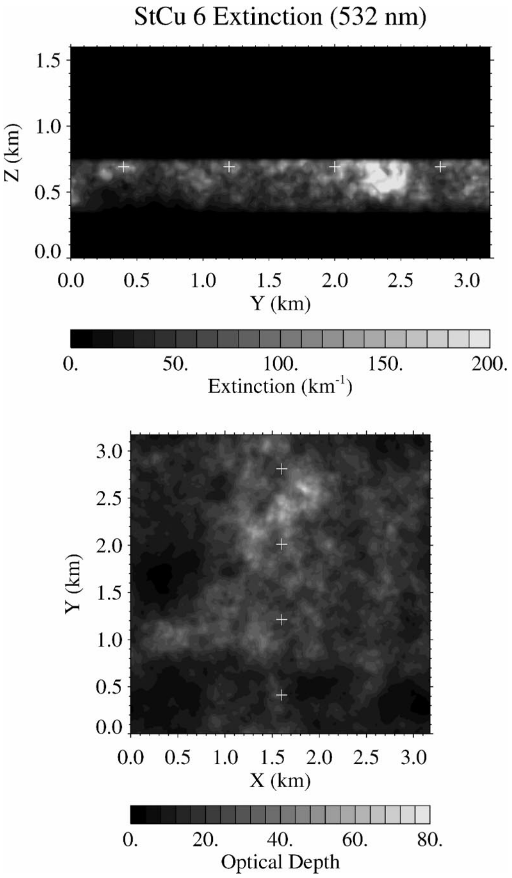

FIG. 5. An Y–Z cross section of extinction and X–Y plot of optical depth for another of the 100 stochastic cloud fields used in the in situ lidar simulations. This cloud field is quite different from the one in Fig. 4, and serves to illustrate the wide range of simulated fields.

$+Z$ and $-Z$ directions (up and down). The detector field of view is ±28.6° (0.50 rad), and its area is 20 cm^2. The simulated lidar signal is accumulated from 0.125 μs until 32 μs with time bins spaced at factors of $\sqrt{2}$. There is molecular Rayleigh scattering in addition to cloud droplet scattering throughout the domain from the surface to 2-km height. There is Lambertian surface reflection with the albedo for each field randomly chosen between 0.05 and 0.25 (i.e., an unknown but fairly dark surface). There are 10^7 photon trajectories in each simulation.

Figure 6 plots four in situ lidar simulated time series from the two cloud fields shown before. As expected from diffusion theory, the signal from the thinner cloud (StCu6) falls off much more rapidly than from the thicker cloud (StCu21). The two time series for StCu21 illustrate how the signal at different times responds to the extinction at different distances from the lidar. The signal for $y = 2.8$ km starts out larger than the signal for $y = 2.0$ km because the local extinction is greater at $y = 2.8$ km. On average the extinction around $y = 2.0$ km increases with distance, while the extinction around $y = 2.8$ km decreases, which results in the two lidar time series having the same strength after about 1.0 μs. The time series for upward- and downward-facing detectors (StCu6) illustrates how the distance to the cloud boundaries affects the lidar signals. After about 0.5 μs the signal for the upward-pointing detector is lower than that for the downward-viewing detector because the lidar is close to the cloud-top boundary. The loss of photons from the top boundary causes the net flux to be upward, which means that more photons are going up than down.

The in situ lidar simulations described in this paper ignore the effect of photon absorption and scattering by the airplane platform. A special simulation is designed to test whether this assumption is warranted. The main property of the aircraft that is important for the in situ lidar photons is the total surface area of the platform. Thus we model the platform as a rectangular surface 15 m (in X) $\times$ 4 m (in Y) oriented horizontally. The center of this winglike surface is 2 m to the left ($-X$), 4 m aft ($-Y$), and 1 m below ($-Z$) the laser location. The albedo of the platform is 0.6, and when photons reflect they do so isotropically (Lambertian surface). Since both sides are active the total surface area is 120 m^2, which is roughly the surface area of a Learjet. Figure

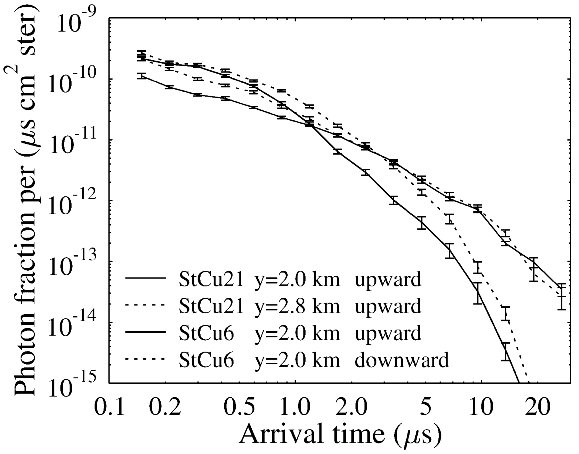

FIG. 6. Simulated in situ lidar time series for upward-pointing detectors at two locations in cloud field StCu21 and upward- and downward-viewing detectors at one location in field StCu6. The error bars indicate the uncertainty due to Monte Carlo noise.

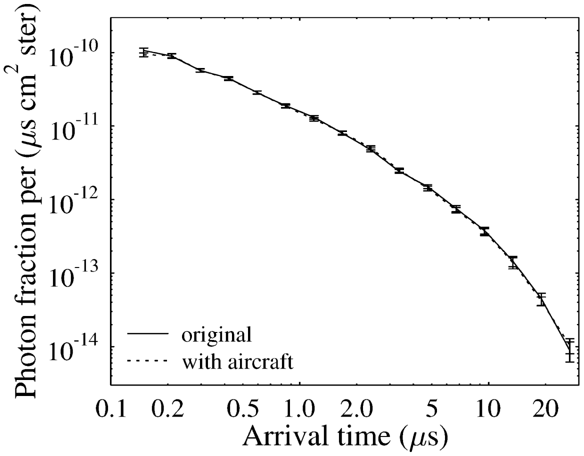

FIG. 7. Simulated in situ lidar time series for the downward-pointing detector at $y = 2.0$ km in field StCu21 with and without the effect of the aircraft platform.

7 shows one in situ lidar time series with and without the effect of the airplane surface. The differences between the two curves are small compared to the Monte Carlo noise, though the difference in the first time bin may be real.

d. Cloud property retrievals

One purpose of the in situ lidar is to measure volume-averaged extinction, but how should the volume average be defined? We choose a Gaussian-weighted volume average extinction, since from diffusion theory the photon density in a uniform medium has a Gaussian spatial pattern. The Gaussian-weighted volume-averaged extinction, β_σ, is defined by

$$\beta_\sigma = \int \beta(x_0 + x, y_0 + y, z_0 + z) \times \frac{1}{(2\pi\sigma^2)^{3/2}} \exp\left[-\frac{(x^2 + y^2 + z^2)}{2\sigma^2}\right] dx\, dy\, dz, \quad (11)$$

where $\beta(x, y, z)$ is the extinction field defined in x, y, z coordinates, and σ is the rms radius of the Gaussian pattern around point (x_0, y_0, z_0). Thus the averaging volume is a fuzzy-edged spherical region with most of the influence contained within a distance of 2σ from the center. Since the laser beam shoots away from the lidar and the photons take about $1/(1 - g)$ or ≈ 7 scatterings to become isotropic, the center of the volume sampled by the in situ lidar is shifted somewhat in the direction of the laser beam. Some results shown later have the center of the Gaussian pattern shifted by $0.15/[(1 - g)\beta]$ (20 m for $\beta = 50$ km^{-1}), which gave the greatest correlation between the in situ lidar signal and the average extinction in a coarse search.

Figure 8 shows the relationship between the volume-averaged extinction at three scales (25, 50, and 100 m) and the simulated in situ lidar signal sampled at three time bins (centered on 0.6, 1.2, and 2.4 μs). The figure shows that the volume-averaged extinction at a particular scale is correlated well to the lidar signal at a particular time and less correlated to the signal at other times. For example, the 50-m scale extinction is best correlated to the 1.2-μs sampled time.

The relatively smooth nature of the in situ lidar return time series suggests that the information content could be extracted by fitting with a simple function. Considering the power-law times exponential behavior from the diffusion model, a form of $p(t) = a' t^{-b} \exp(-ct)$ seems appropriate. The curve fits are performed in log space so that a linear least squares program can be used and so as to not overemphasize the early portion of the signal. Therefore, the functional form used in the lidar signal fit is

$$\ln[p(t)] = a - b \ln(t) - ct, \quad (12)$$

where $p(t)$ is the photon fraction signal as a function of time. The signal uncertainties for the linear least squares are obtained from the Monte Carlo standard deviation estimates, e, which are translated to fraction error (e/p) for the log space fit. The first part of the time series deviates from the power-law behavior due to the distance between the lidar and detectors, and it also represents a small averaging volume, so only bins after a minimum time $t_{\min}$ are used for the fitting. Over the 400 cases (4 positions in 100 cloud fields) the median reduced χ^2 of the fit is 3.5 and 3.2 (for up and down detectors, respectively) for $t_{\min} = 0.2$ μs, and 1.9 and 1.7 for $t_{\min} = 0.5$ μs, indicating that ignoring the first 0.5 μs of the time series results in a better fit. These reduced χ^2 values show that the bulk of the in situ lidar signal is fit well with the power-law times exponential function, meaning that just three numbers (a, b, c) represent most of the available information. The deviations from the functional form are significant (above the cur-

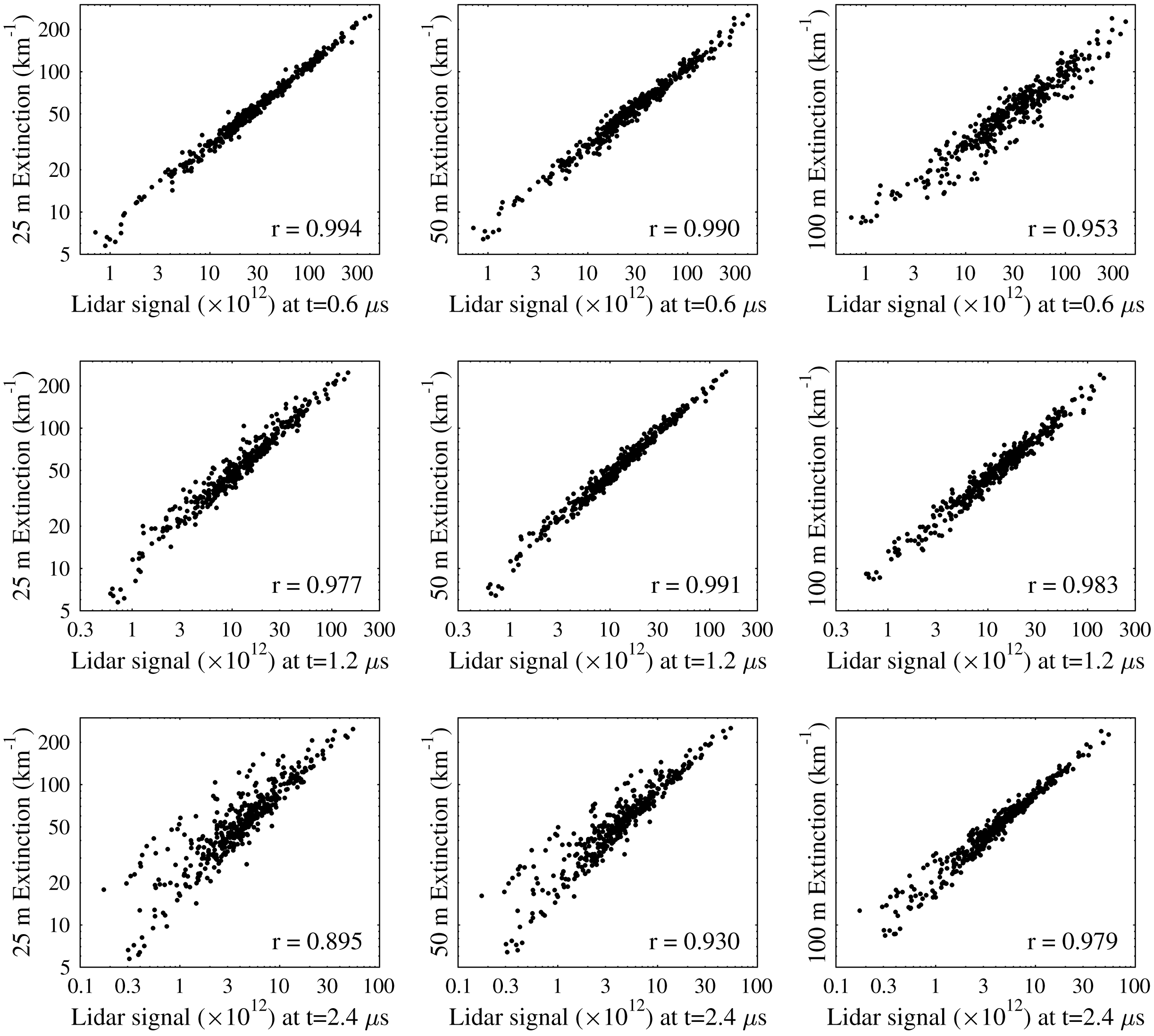

FIG. 8. The Gaussian-weighted volume-averaged extinction for three sized volumes vs the in situ lidar signal sampled at three different times for the stratocumulus simulation. The linear correlation coefficient r (in log space) is listed for each graph.

rent amount of Monte Carlo noise), presumably due to cloud inhomogeneities, so there is some additional information contained in these time series. For fits to the average of the up and down detector time series, the mean of the exponent b is 1.14, while the standard deviation is 0.32. This range for the exponent is consistent with the diffusion theory solution for finite clouds, considering that the diffusion theory was developed for uniform clouds.

A retrieval algorithm was developed using a neural network (NN) to relate the fit parameters a, b, and c to the volume-averaged extinction and cloud thickness. This neural network is simply used as a nonlinear regression technique to fit the output (e.g., log of averaged extinction at four different scales) to the input (a, b, c). The neural network algorithm is modeled after NN-fit (available online at http://www.gch.ulaval.ca/~nnfit). The neural network consists of two layers of neuronal units: hidden units connected to the inputs and output units connected to the hidden units. Each unit multiplies its inputs by a set of weights and the sum is then nonlinearly transformed by the sigmoid function $[f(z) = 1/(1 + e^{-z})]$ to produce the unit output. Thus, the weights of all the units are the ''regression'' coefficients that are adjusted to minimize the rms error between the predicted outputs and the desired outputs. A conjugate gradient routine is used to perform this minimization. The neural net is trained on a random portion of the dataset, while the rest of the dataset is used to test the network. This is important because a neural network can ''overfit'' the data in a way that does not generalize. The overfitting problem is much like fitting an nth degree polynomial to n datapoints: the resulting curve will go through each datapoint, but will most likely give bizarre results at

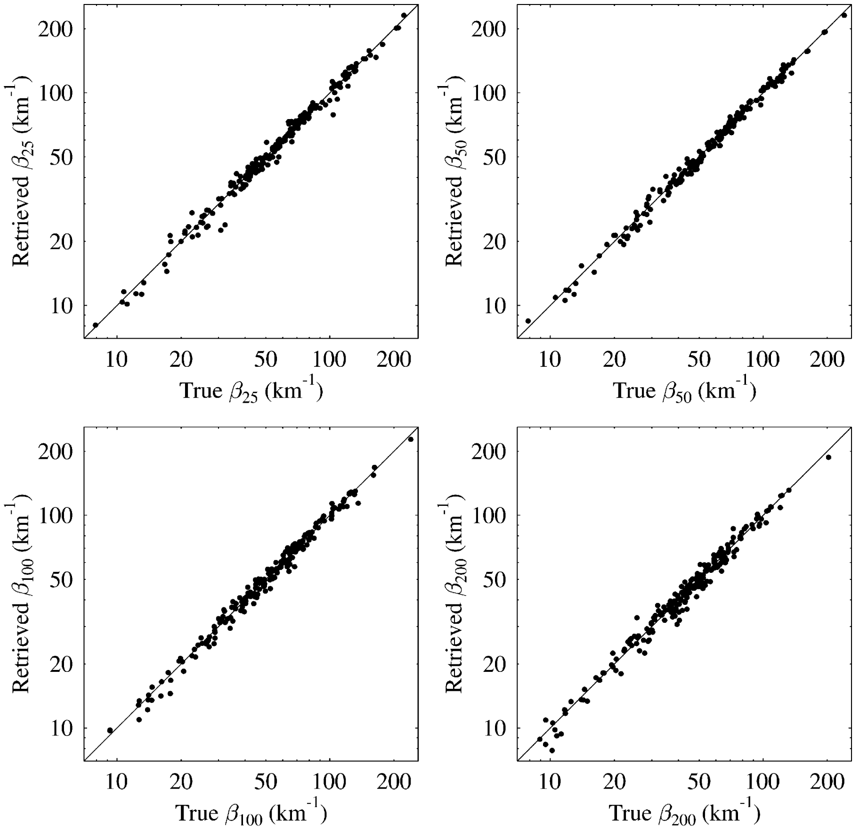

FIG. 9. The in situ lidar volume-averaged extinction retrievals vs the true extinction values. Here β_σ is the volume-averaged extinction weighted by a Gaussian pattern with an rms radius of σ m. Shown are 200 cases from the stochastic stratocumulus simulation used to test the neural network.

other locations. Overfitting is prevented by early stopping, that is, stopping the minimization iterations when the error in the testing dataset stops decreasing.

Half of the 400 cases are used to train the neural net. Different networks are trained for predicting log extinction at four scales ($\sigma = 25, 50, 100, 200$ m), log optical depth at four Gaussian-weighted horizontal scales ($\sigma = 50, 100, 200, 400$ m), and cloud geometric thickness and cloud relative airplane height. The inputs in each case are the three parameters (*a, b, c*) fit to the in situ lidar signal for the up and down detectors (total of six input parameters). There are usually 20 hidden units in the network.

The volume-averaged extinction retrieval accuracy for four scales ranging from $\sigma = 25$ to $\sigma = 200$ m is illustrated in Fig. 9. The rms retrieval accuracies are listed in Table 2. A typical rms retrieval error is about 8%, which is much smaller than the range of extinction in the simulated clouds (the standard deviation is a factor of 1.8). The errors are usually lowest for the $\sigma = 50$ m and $\sigma = 100$ m volume averages. The retrieval errors are slightly lower when the averaging volume is offset in the direction of the laser beam, which is the experiment shown in Fig. 9. Another experiment shows that the retrieval error is somewhat lower when the neural network is trained directly with 28 time series values (14 bins for two detectors) instead of the parameters of the power-law times exponential function fit. The first set of retrieval accuracies are shown for no calibration error. Of course, a real instrument will have calibration uncertainty. This is modeled by multiplying the in situ lidar signals input to the neural network retrieval algorithm by a constant ‘‘calibration error factor’’ of 1.2 (20% error) or 1.5 (50% error). Table 2 shows the surprising result that the retrieval error is only about half of the calibration error (50% calibration error gives about 25% retrieval error).

The average extinction for different-sized volumes are correlated, of course, but is this correlation the reason why the in situ lidar technique can accurately retrieve the extinction at different scales? Figure 10 shows that while there is reasonable correlation between nearby scales, the correlation is quite poor as the size of the averaging volumes diverge. This figure indicates that the in situ lidar really is able to retrieve the cloud extinction averaged over different distances in inhomogeneous clouds.

The exponential behavior of the in situ lidar signal

TABLE 2. The in situ lidar rms retrieval accuracy of ln (β_σ).*

N_{case}	Dataset	β_{25}	β_{50}	β_{100}	β_{200}	Experiment
200	Training	0.074	0.064	0.062	0.077	No volume offset
200	Testing	0.082	0.068	0.072	0.091	
200	Training	0.067	0.049	0.050	0.066	With volume offset
200	Testing	0.074	0.059	0.062	0.081	
200	Training	0.049	0.048	0.045	0.055	Retrieval from 28 time bins with no volume offset
200	Testing	0.060	0.062	0.071	0.096	
400	All cases	0.070	0.054	0.056	0.074	No calibration error
400	All cases	0.127	0.118	0.122	0.129	20% calibration error
400	All cases	0.250	0.245	0.250	0.247	50% calibration error
200	Testing	0.632	0.618	0.589	0.580	Standard deviation of cases

* β_σ is the volume-averaged extinction weighted by a Gaussian with rms radius of σ. Since they are small the rms retrieval accuracies of ln(β) may be interpreted as rms fractional errors in β. For comparison the variability (std dev) of lnβ is also listed. The accuracy of the 200 cases used for training the neural network are listed separately from the 200 cases used to test the neural network for each of several experiments. The last experiment section lists the retrieval accuracy for all 400 cases with varying factors of calibration error.

due to the photon diffusion bubble reaching the cloud boundaries allows the retrieval of cloud thickness. Figure 11 shows that cloud thickness can indeed be retrieved and that the error is smaller for the thinner clouds. The different responses of the upward- and downward-pointing detectors allows the in situ lidar to measure the cloud relative altitude of the airplane as shown in Fig. 11. Table 3 lists the retrieval errors. The cloud thickness and airplane height retrievals are almost insensitive to the lidar calibration, since they depend on the shape of the lidar time series. The simulations assumed little knowledge of the surface reflection effect, with the albedo ranging from 0.05 to 0.25 and varying cloud-base heights. Figure 12 shows the results of an experiment testing the effect of this range of surface albedo on the lidar time series. There is a significant difference only in the latter part of the time series, with the brighter surface having a larger signal as fewer photons are lost from the system. The time at which the surface albedo effect becomes important depends on the height of the cloud base, and higher base clouds will have less sensitivity to surface albedo. Since the cloud thickness is determined from these latter times, we expect the cloud thickness retrievals to be improved if there is better knowledge of the surface albedo. The cloud thickness retrievals should also improve if the airplane is flown near the middle of the cloud.

Given that the in situ lidar can accurately retrieve volume-averaged extinction and cloud thickness, it should also be able to sense the cloud optical depth averaged over a suitable area. The optical depth is averaged using two-dimensional Gaussian weighting functions (specified by rms radius σ) centered on the lidar. Figure 13 shows the retrieval accuracy for the $\sigma = 200$-m scale of area-averaged optical depth, while Table 4 lists the retrieval accuracy for all four scales. Two experiments are shown: one for all cases and one for those cases in which the airplane is near the center of the cloud. As one might expect, the accuracy of the optical depth retrieval increases substantially when the airplane is near the cloud middle. The rms optical depth retrieval error at the 200-m scale for these cases is about 8%, while the simulated variability is a factor of 2.0. The sensitivity of the optical depth retrieval to lidar calibration is similar to the extinction retrieval.

Given that only three parameters fit to the in situ lidar time series for each detector are input to the neural network retrieval, it is appropriate to think that at most three cloud properties can be retrieved. These three properties can be thought of as the volume-averaged extinction at some scale, the rate at which the extinction changes with the scale of the averaging volume, and the distance to the cloud boundaries.

4. Prototype in situ lidar demonstration

The prototype in situ lidar designed and built by SPEC, Inc., consists of two basic components: a high-powered, pulsed Nd:YAG frequency doubled laser operating at 532 nm and a photomultiplier tube (PMT) detector and associated control and recording electronics. The YAG laser emits a 5-ns-long pulse of green light 15 times per second. At full power the energy in a pulse is 105 mJ, as measured by the manufacturer.

The heart of the detector is a Hamamatsu H7680-01 gated PMT module consisting of a photomultiplier tube, a drive circuit for high-speed gated operation, and a high-voltage power supply. The PMT does not have the 10^6 dynamic range of the in situ lidar return signal. Therefore, a simple solution for the prototype instrument was to measure different parts of the return signal in different runs. The control circuitry allows the gain of the PMT to be varied manually. The Q-synch pulse from the laser triggers a programmable delay circuit that turns on the PMT at a manually specified later time to avoid saturation during the earlier high power portion of the return. A transimpedance amplifier produces a voltage proportional to the PMT output current. The laser Q-synch pulse also triggers a digital oscilloscope to take 500 samples at 0.2-μs intervals of the voltage, which is proportional to the photon flux impinging on the PMT. Collection optics focus the lidar return signal

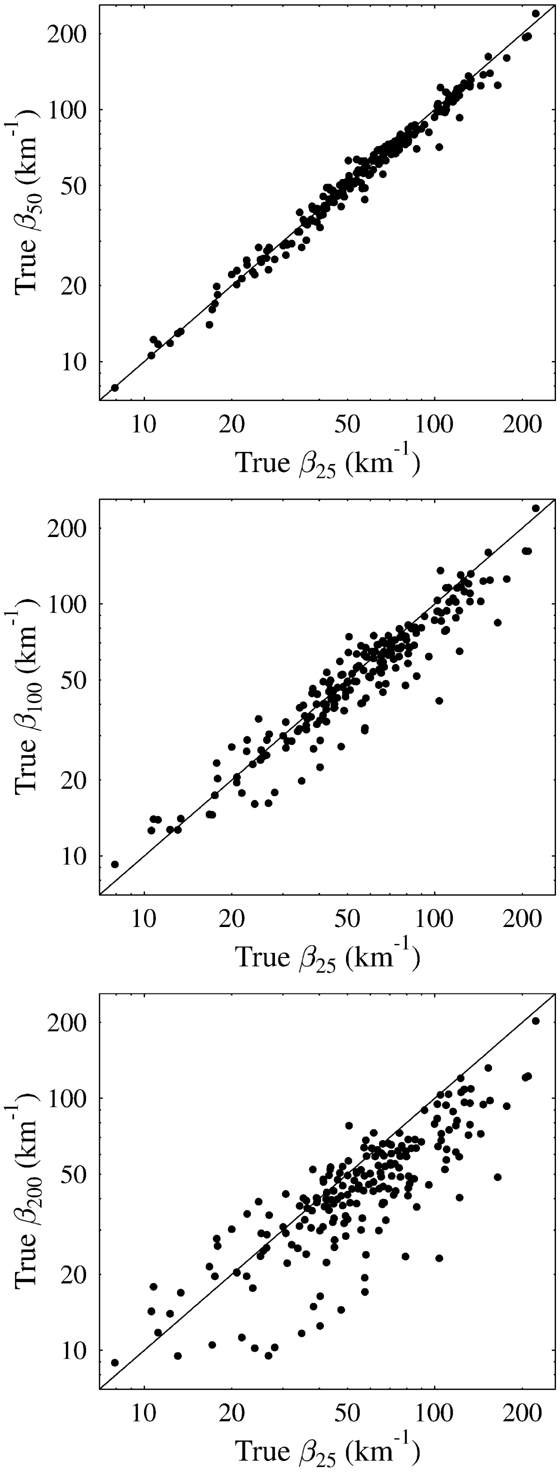

FIG. 10. The relationships between the true Gaussian-weighted volume-averaged extinction at different scales.

onto the PMT cathode. The field of view of the optics was measured to be ±28.5°. A spectral filter with a center wavelength of 550 nm and a full-width at half-maximum of 60 nm is used to reject background light.

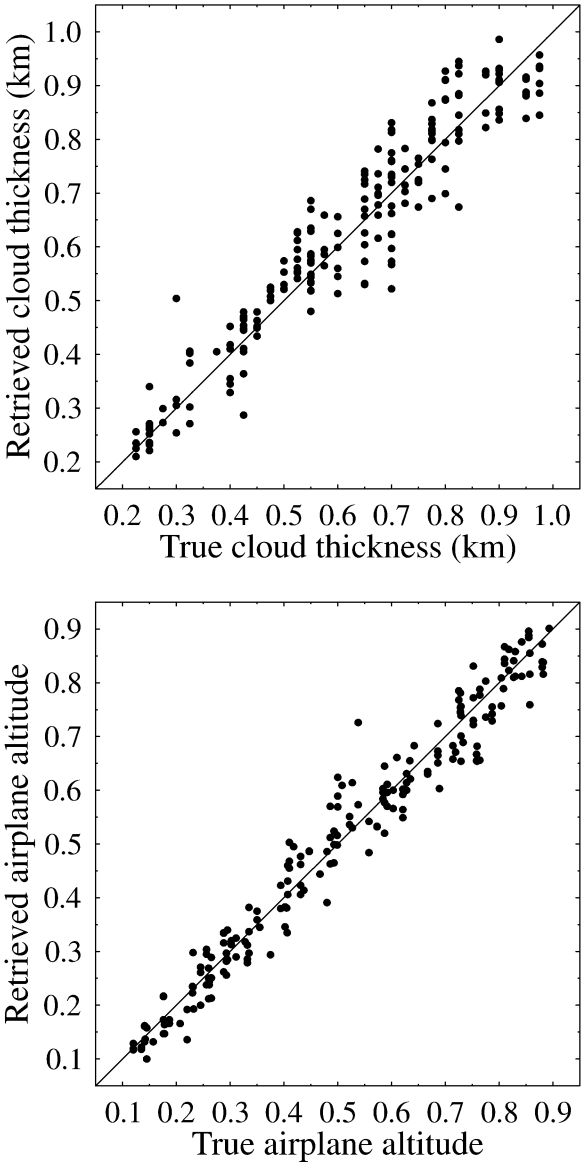

FIG. 11. The in situ lidar cloud thickness retrievals vs the (top) true thickness values and (bottom) retrieved vs true cloud airplane altitude. The airplane altitude is in terms of the fraction from cloud base to top. The 200 cases from the simulation used to test the neural network are shown. The quantization in true cloud thickness is due to the 25-m spacing of the simulated cloud layers.

TABLE 3. The in situ lidar rms retrieval accuracy of geometric cloud thickness (Δz, km) and airplane altitude relative to cloud boundaries (Z_{plane}).*

N_{case}	Dataset	ΔZ	Z_{plane}	Experiment
200	Training	0.056	0.048	No volume offset
200	Testing	0.063	0.044	
400	All cases	0.059	0.046	No calibration error
400	All cases	0.062	0.047	20% calibration error
400	All cases	0.070	0.050	50% calibration error
200	Testing	0.202	0.228	Std dev of cases

* Further explanation of the table is contained in Table 2.

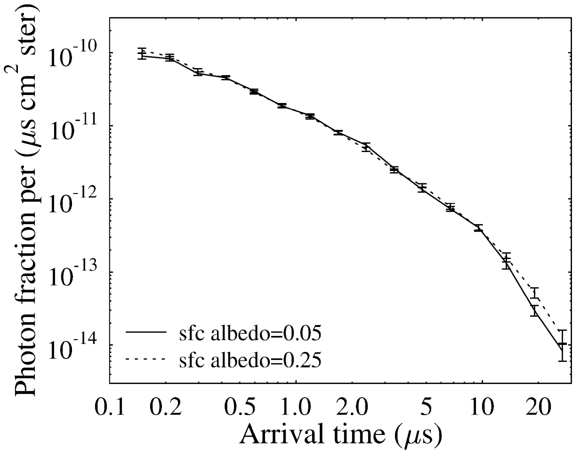

FIG. 12. Simulated in situ lidar time series for downward-pointing detectors at $y = 2.0$ km in field StCu21 for surface albedo of 0.05 and 0.25.

The detector was operated with a 10% neutral density filter to prevent signal saturation at the beginning of the lidar return signal.

A field experiment to test the prototype in situ lidar was carried out at the Storm Peak Laboratory (SPL) located on the top of Mt. Werner (3220-m elevation) above Steamboat Springs. The SPL is an atmospheric science research facility operated by the Desert Research Institute of the University of Nevada (Borys and Wetzel 1997; http://stormpeak.dri.edu/). During the winter months the lab is often enveloped in cloud. The prototype in situ lidar was installed on the lab roof on 1 April 2002. The only cloud event during the 2-week experiment period was on the night of 10–11 April.

A rapidly moving short wave passed through the SPL area from about 1800 UTC 10 April until 1800 UTC 11 April. The research team arrived at the SPL around 0200 UTC 11 April while the laboratory was experiencing moderate to heavy snowfall, a westerly wind of 10–15 m s^{-1} and a temperature of -2°C. SPL is at 690 mb and the local temperature was the same as the temperature at 700 mb based on the 1200 UTC National Weather Service analysis. The *GOES-8* brightness temperature was 223 K (-50°C), which corresponds to a

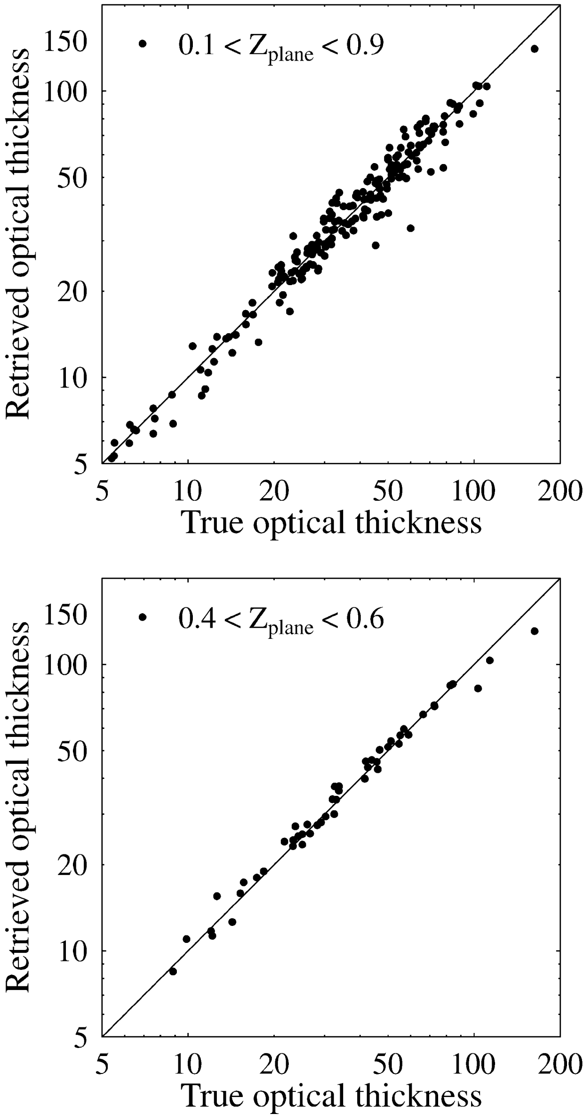

FIG. 13. The in situ lidar area-averaged optical depth retrievals vs the true optical depth values. The optical depth is weighted by a Gaussian pattern with an rms radius of 200 m. (top) The 200 testing cases over all aircraft altitudes, (bottom) 50 cases with the cloud relative aircraft height between 40% and 60%.

TABLE 4. The in situ lidar rms retrieval accuracy of 1n (τ_σ).*

N_{case}	Dataset	τ_{50}	τ_{100}	τ_{200}	τ_{400}	Experiment
200	Training	0.118	0.102	0.093	0.102	No volume offset
200	Testing	0.166	0.149	0.134	0.135	$0.1 < Z_{\text{plane}} < 0.9$
50	Training	0.083	0.063	0.056	0.081	No volume offset
50	Testing	0.112	0.099	0.082	0.091	$0.4 < Z_{\text{plane}} < 0.6$
100	All cases	0.098	0.083	0.070	0.086	No calibration error
100	All cases	0.143	0.132	0.121	0.118	20% calibration error
100	All cases	0.246	0.236	0.218	0.184	50% calibration error
200	Testing	0.709	0.702	0.691	0.676	Std dev of cases

* τ_σ is the area-averaged optical depth weighted by Gaussian with rms radius of σ. The second experiment is to use only those cases in which the cloud relative airplane height is between 0.4 and 0.6. The calibration error tests for the $0.4 < Z_{\text{plane}} < 0.6$ experiment. Explanation of other aspects of the table is contained in Table 2.

cloud-top elevation of approximately 260 mb. There was very little evidence of riming (i.e., supercooled liquid water) on the roof of the laboratory. Thus, the cloud system was deep and developing precipitation in the form of snow at SPL at this time. This regime lasted until about 0700 UTC when the *GOES-8* brightness temperature increased to 260 K (−13°C) and remained in the range of 253 to 260 K (−20° to −13°C) until 1000 UTC. Rapidly moving shortwaves advected over the SPL area in the winter often generate deep cloud systems that initially produce intense snowfall, followed by a rapid lowering of cloud top associated with decreasing precipitation from the supercooled water cloud that engulfs the mountaintop (Borys 2003, personal communication).

During the time period from 0700 to 1000 UTC, observers on the roof of the SPL often recorded dense, but highly variable cloud, with riming on exposed upwind surfaces and no solid precipitation. The laboratory Forward Scattering Spectrometer Probe (Knollenberg 1981), which started operating at 0600 UTC, recorded values of liquid water content from about 0.2 to 0.5 g m^{-3}, with droplet concentrations ranging from 120 to 200 cm^{-3} and an effective droplet radius of 8–10 μm. This corresponded to extinction coefficients ranging from about 40 to 60 km^{-1}. The FSSP is intended for aircraft operation where the airflow is relatively steady and unidirectional. At SPL, the measurements are highly influenced by local conditions (wind direction, velocity, turbulence, and ground obstructions) and cannot be used to directly compare with the volumetric measurements made by the in situ lidar. However, the FSSP measurements, along with the visual observations, can be used to infer that the laboratory was engulfed in a supercooled water cloud with an estimated extinction coefficient of about 40–60 km^{-1}.

On 11 April the in situ lidar was operated systematically from about 0700 to 1000 UTC. To capture the complete dynamic range of the lidar signal, the PMT gain had to be manually adjusted in discrete steps. The operating procedure was to measure 25 time series approximately 0.55 s apart (the maximum rate at which the digital oscilloscope could record) at each gain setting. Fourteen sequences of three or four gain settings were taken at various viewing elevation angles during the 0700–1000 UTC period. The manual setting of the gain and PMT time delay meant that there were typically 2 min between successive gain settings. During this time, cloud conditions would change so that the separate gain sections of the in situ lidar signal often do not overlap.

The calibration procedure converts the digital oscilloscope sampled voltages into lidar photon fraction using a system equation approach, rather than with a calibration measurement. The calibration includes the laser pulse energy output, the measured detector field of view and area, the transmission of the neutral density and spectral filters, and the PMT gain from the manufacturers gain curve and the measured PMT control voltage. The mean and standard deviation of the mean in situ lidar signal over the 25 sampled time series at each gain setting are averaged appropriately over log spaced time bins. Only those 0.2-μs samples after the PMT gain stabilizes and with values above the noise level are included in the averages. Figure 14 shows the in situ lidar time series composited from two gain sequences. The prototype lidar signal has a power-law behavior, as expected from the diffusion theory for a thick cloud. The time series for the gain sequences overlap well in these two examples, which suggests that the cloud extinction was constant over the time required to acquire them. There is some indication of exponential behavior at the end of the lidar time series around 0915 UTC, which may be due to the diffusing photons reaching cloud boundary.

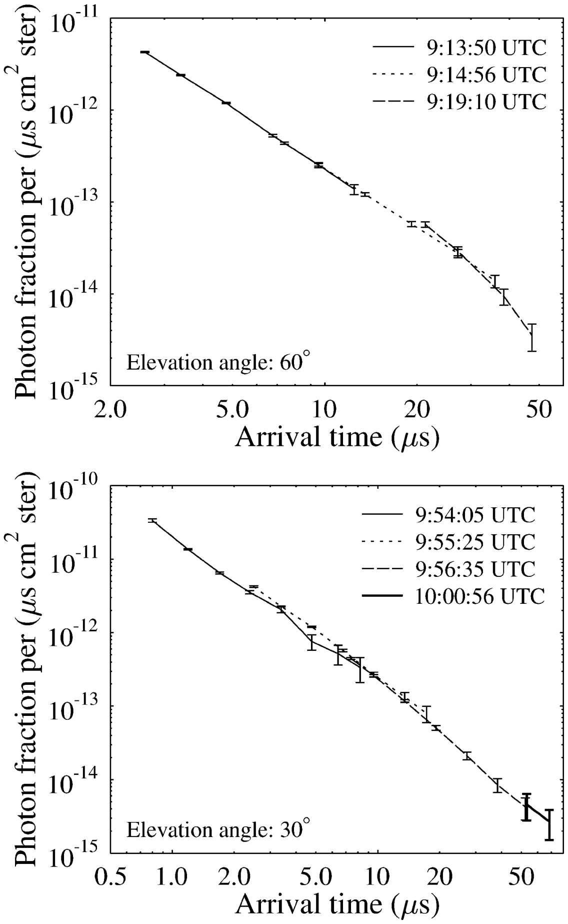

FIG. 14. Two time series from the prototype in situ lidar at SPL on 11 Apr 2002.

We do not attempt to use the curve fitting and neural net retrieval procedure developed in section 3. The separate time series for each gain setting make the curve fitting procedure impractical. We are also rather uncertain of the calibration of the prototype in situ lidar, and we have no validation of the volume-averaged extinction.

Nevertheless, we can use Fig. 8 to estimate the volume average extinction from the in situ lidar signal at particular times. For the gain section at 0954:05 UTC the photon fraction is 1.36×10^{-11} (μm cm^2 ster)$^{-1}$ at 1.2 μs and 3.5×10^{-12} (μm cm^2 ster)$^{-1}$ at 2.4 μs. The corresponding volume extinctions from a linear regression of Fig. 8 are 56 km^{-1} for a 50-m rms radius volume and 46 km^{-1} for a 100-m rms radius volume. The regression relations from Fig. 8 may not be appropriate due to the effects of reflection from the snow- and tree-covered mountain surface. The prototype in situ lidar signals have no or a very slight exponential decay region, which means we cannot retrieve the cloud thickness, but does indicate that the cloud was thicker than 1 km.

5. Two wavelength in situ lidar simulations

The simulations previously described showed that an in situ lidar operating at a single nonabsorbing wavelength such as 532 nm can accurately measure the volume average cloud extinction surrounding the lidar. In analogy with dual-wavelength solar reflectance remote sensing methods (Twomey and Cocks 1982; Nakajima and King 1990), it seems likely that the addition of a second wavelength at which cloud droplets absorb light would allow measurement of effective radius and liquid water content in warm clouds.

What is the appropriate choice for the second wavelength? The single scattering albedo for typical cloud droplets should be in the range from 0.95 to 0.995 so that there is a measurable absorption signal while still having substantial multiple scattering. Absorption by water vapor should be very low to avoid dependence on the water vapor profile. Shorter wavelengths are better in terms of laser and detector technology. Wavelengths around 1550 nm are the shortest wavelengths with adequate droplet absorption and low water vapor absorption. The transmission at 1550 nm of a 1-km saturated air path at 280 K and 900 mb is 0.99964 (line-by-line radiative transfer model calculation). The droplet single scattering albedo at 1.55 μm ranges from 0.995 at effective radius $r_e = 5$ μm to 0.985 at $r_e = 15$ μm. The required technology is much more difficult in the near infrared than visible. High laser pulse energy might be achieved with a deuterium gas Raman shifting cell, which converts the Nd:YAG 1064 nm fundamental to 1560.7 nm. Photomultiplier tubes do not work at 1550 nm, but a liquid nitrogen cooled avalanche photo diode detector with an efficiency of about 10% at 1550 nm is available.

Simulations of a 1550-nm wavelength in situ lidar are performed identically to the previous 532-nm simulations. The same instrument geometry and the same fractal stratocumulus clouds are used, but the optical properties are computed at 1550 nm. Figure 15 illustrates the difference between the lidar time series at 532- and 1550-nm wavelengths. As expected from diffusion theory for an absorbing medium, the 1550 nm has a more pronounced exponential fall off at later times. The 1550-nm signal is actually larger than the 532-nm signal at early times, mainly due to lower asymmetry parameter at 1550 nm ($1 - g$ is 13.2% higher at 1550 nm for $r_e = 10$ μm).

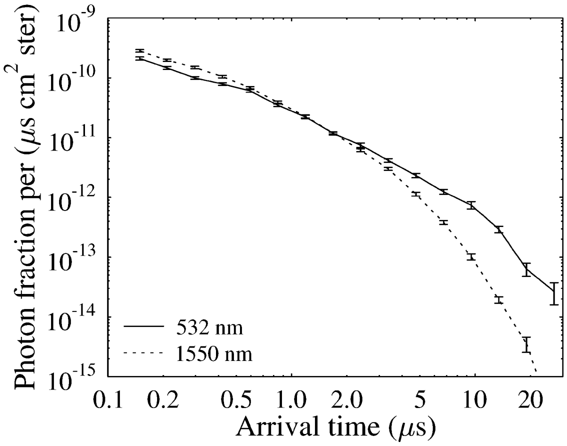

FIG. 15. Simulated in situ lidar time series for upward-pointing detectors at $y = 2.8$ km in field StCu21 for lidars operating at 532- and 1550-nm wavelengths.

As described in section 3d, a neural network is trained with half of the 400 cases to retrieve log liquid water content and effective radius. The input to the network is the a, b, c parameters fit to the average of the upward- and downward-pointing detectors. Two experiments are performed: the first with the six input parameters from the 532- and 1550-nm lidars, and the second with the three inputs from only the 532-nm lidar. Figure 16 shows that the retrieval accuracy is quite good for two wavelength lidars, but degrades considerably using only the 532-nm wavelength, particularly for effective radius. The retrieval accuracy for all four volume scales is listed in Table 5. The rms accuracy is between 10% and 12% for LWC and under 0.5 μm for effective radius for the dual wavelength combination. There is still some ability to retrieve LWC with a single wavelength because extinction and LWC are correlated, but there is little skill in retrieving effective radius with a single wavelength.

These retrieval simulations of liquid water content and droplet effective radius are very promising for the dual wavelength in situ lidar concept. Is there any further information to be gained from a third wavelength? The difference between the index of refraction of water and ice in this spectral region has prompted suggestions that the ice fraction in mixed phase clouds could be determined by remote sensing (Pilewskie and Twomey 1987). To separate the absorption effect of liquid droplets from ice particles requires two absorbing wavelengths that have distinct amounts of absorption by water and ice. The ratio of the bulk absorption coefficient of ice to that of water is 3.58 at 1550 nm. A third in situ lidar wavelength near 1760 nm, where the absorp-

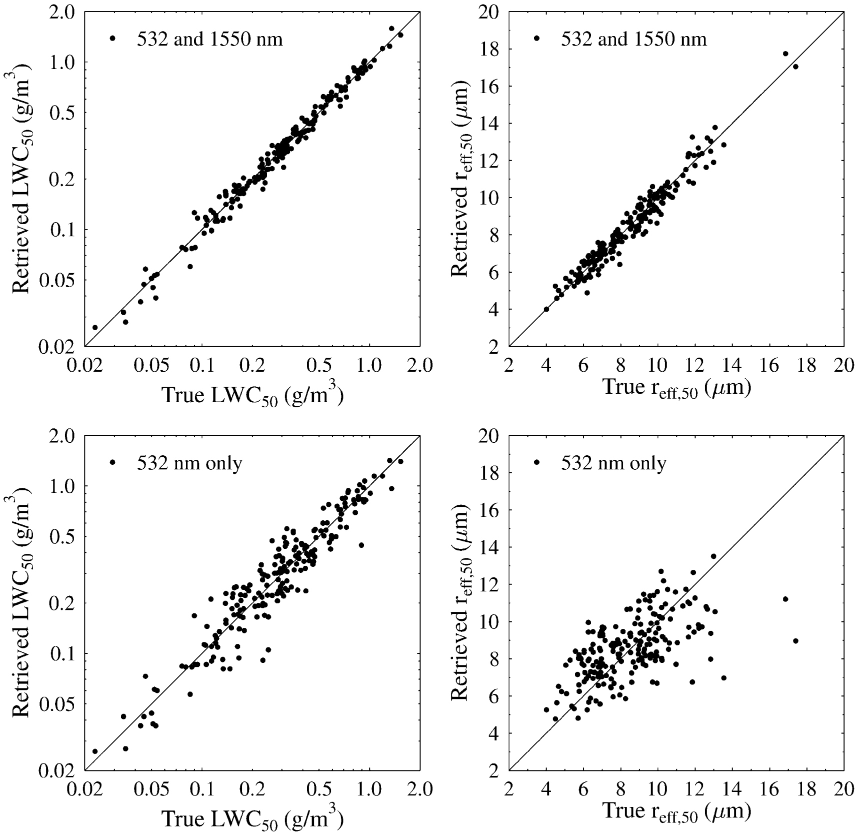

FIG. 16. The in situ lidar volume-averaged LWC and effective radius (r_{eff}) retrievals vs the true values for the $\sigma = 50$ m scale for the two experiments. The 200 cases from the simulation used to test the neural network are shown.

tion coefficient ratio is 1.16 and the 1-km saturated path transmission is 0.99, may add the ability to measure ice water content (IWC) and particle size. Appropriate ice crystal scattering phase functions would need to be added to the retrieval forward modeling, and we would expect larger errors in retrieving IWC compared to LWC due to the greater uncertainty in asymmetry parameter g for ice particles than for liquid cloud droplets.

6. Summary and conclusions

The in situ lidar technique is a new method for measuring extinction averaged over regions hundreds of meters in diameter in optically thick water clouds. The technique envisions high power laser pulses being emitted horizontally from an aircraft flying inside a cloud and wide-field-of-view detectors pointing upward and downward measuring the time series of the number of returned photons. In situ lidar is an in situ remote sensing technique, combining the advantages of in situ cloud probes and remote sensing. It has much of the accuracy and directness of in situ cloud probes, but the large volume sampling of remote sensing. Of course, it has the limited geographic coverage of any aircraft-based method. The large sampling volume of the in situ lidar

TABLE 5. The in situ lidar rms retrieval accuracy of ln (LWC$_\sigma$) and r_{e}^{e}.

Dataset	LWC$_{25}$ (log)	$r_{e,25}$ (μm)	LWC$_{50}$ (log)	$r_{e,50}$ (μm)	LWC$_{100}$ (log)	$r_{e,100}$ (μm)	LWC$_{200}$ (log)	$r_{e,200}$ (μm)	Experiment
Training	0.108	0.45	0.096	0.42	0.091	0.40	0.103	0.44	532 and 1550 nm
Testing	0.121	0.53	0.104	0.49	0.106	0.45	0.120	0.52	
Training	0.268	1.97	0.250	1.96	0.252	1.97	0.283	1.99	532 nm only lidar
Testing	0.276	1.87	0.257	1.80	0.250	1.75	0.265	1.69	
Testing	0.848	2.30	0.800	2.20	0.704	2.04	0.593	1.92	Std dev of cases

* LWC$_\sigma$ is the volume-averaged liquid water content weighted by a Gaussian with an rms radius of σ, while $r_{e,\sigma}$ is the effective radius calculated from the ratio of the volume-averaged LWC and extinction. For comparison the variability (std dev) of the LWC and r_e is also listed. The accuracy of the 200 cases used for training the neural network are listed separately from the 200 cases used to test the neural network for experiments using the dual and single wavelength lidars.

technique will allow much more precise validation of cloud remote sensing methods than possible now with the small sampling volumes of current cloud probes.

A diffusion theory calculation predicted that the in situ lidar time series for an infinite uniform nonabsorbing medium is proportional to $[(1 - g)\beta/ct]^{3/2}$, where t is time, c is the speed of light, β is the volume extinction coefficient, and g is the asymmetry parameter. The addition of absorption multiplies this power-law behavior with an exponential function, $e^{-(1-\omega_0)\beta ct}$, where ω_0 is the single scattering albedo. When the bubble of diffusing photons is comparable to the size of the cloud, the loss of photons from the cloud causes the in situ lidar time series to decrease exponentially with a timescale proportional to the square of the cloud thickness.

Retrieval simulations were performed to determine how accurately the in situ lidar can measure extinction, optical depth, and cloud thickness in realistic warm stratocumulus clouds. Three-dimensional inhomogeneous fractal clouds were simulated with a Fourier noise filtering algorithm that generates partially correlated liquid water content and droplet number concentration fields. The 100 cloud fields generated, with 25-m pixels and 3200-m domain size, had a wide range of thickness, mean liquid water path, variability, smoothness, and mean droplet concentration. A Monte Carlo model simulated the 532-nm wavelength in situ lidar time series signal for upward- and downward-pointing detectors at four positions along a randomly chosen flight altitude in each cloud. The lidar time series, $p(t)$, are reasonably well fit by the function $\ln[p(t)] = a - b \ln(t) - ct$ (inspired by the diffusion theory solution). A retrieval algorithm is developed by training a neural network to predict the volume average extinction (Gaussian-weighted average at four scales) from the a, b, and c parameters for each detector. Half of the 400 cases are used to train the neural net, and half are used to test the retrieval accuracy. The rms fractional error in extinction ranged from 6% to 8% depending on the volume scale. The in situ lidar was able to retrieve the cloud thickness with about 60-m rms accuracy (thicknesses ranged from 200 to 1000 m). Using only those airplane altitudes near the center of the cloud gave an the optical depth retrieval accuracy of under 10%. The in situ lidar technique is only weakly dependent on the calibration accuracy with a 50% calibration error giving an extinction error of 25% and causing very little increase in cloud thickness error. These retrieval accuracies are applicable to overcast warm (liquid) stratocumulus clouds with well-defined top and base altitudes. The extinction retrieval accuracy should be comparable for any liquid cloud, as the extinction in this simulation ranged from 5 to 250 km^{-1} and the cloud mean droplet concentration ranged from 50 to 300 cm^{-3}.

Simulations were also performed for a potential dual-wavelength in situ lidar with wavelengths at 532 and 1550 nm. The absorption at 1550 nm is proportional to the cloud droplet radius, which allows the accurate retrieval of liquid water content and effective radius. The simulated rms accuracy of LWC ranges from 10% to 12% depending on scale, while the effective radius accuracy is about 0.5 μm.

A ground-based prototype in situ lidar was tested in April 2002 at the Storm Peak Laboratory on Mt. Werner above Steamboat Springs, Colorado. The 105 mJ per pulse 532-nm YAG laser pointed vertically, while the photomultiplier tube detector with a ±28° field of view could be pointed at any angle. During a cloud event on the night of 11 April, the lidar measured time series having the expected power-law behavior with detectable signal out beyond 40 μs.

SPEC, Inc., has received a NASA contract to build and test a prototype airborne in situ lidar. Figure 1 illustrates the installation envisioned for the SPEC operated Learjet. After passing through diverging optics for eye safety, the 532-nm wavelength YAG laser beam will exit out a cabin window traveling horizontally. The two detectors will be mounted in a Particle Measuring Systems canister on the Learjet tiptank on the opposite wing. The detector fore optics will have 50-mm-diameter lenses with ±28° fields of view pointing upward and downward. The light for each detector will be passed through an interference spectral filter to block some of the nonlaser background light. The solar background is so overwhelming that it will probably require an expensive atomic line filter (e.g., Chen et al. 1993) to operate during the daytime, and the in situ lidar will initially be operated at night. To cover the large dynamic range of the in situ lidar signal two types of detectors will be used. The high-level part of the signal will be measured with an avalanche photodiode, while the lower-level part will be measured with a photomultiplier tube. Initial tests of the instrument will be performed on the ground at the Storm Peak Laboratory, while later tests will occur on the Learjet aircraft in a variety of cloud types. The performance of the airborne in situ lidar will be evaluated by comparing extinction retrievals in relatively homogeneous clouds with averages of local extinction determined from a Forward Scattering Spectrometer Probe (FSSP-100) (Knollenberg 1981) and a cloud extinctometer (Zmarzly and Lawson 2000) on the Learjet research aircraft.

Acknowledgments. We are grateful to Dr. Randy Borys, Director of the DRI Storm Peak Laboratory (http://stormpeak.dri.edu/), for providing valuable technical and logistical support. Financial support was provided by NASA SBIR phase 1 Contract NAS5-01193 and phase 2 Contract NAS5-02111 to SPEC, Inc. Financial support was also provided (for KFE and WJW) by the Environmental Sciences Division of the U.S. Department of Energy (under Grant DE-A1005-90ER61069 to NASA Goddard Space Flight Center) as part of the ARM program.

REFERENCES

Askebjer, P., and Coauthors, 1997: UV and optical light transmission properties in deep ice at the South Pole. *Geophys. Res. Lett.,* **24,** 1355–1358.

Baker, B. A., 1992: Turbulent entrainment and mixing in clouds: A new observational approach. *J. Atmos. Sci.,* **49,** 387–404.

Barker, H., and J. A. Davies, 1992: Solar radiative fluxes for stochastic, scale-invariant broken cloud fields. *J. Atmos. Sci.,* **49,** 1115–1126.

Bissonnette, L. R., and D. L. Hutt, 1995: Multiply scattered aerosol lidar returns: Inversion method and comparison with in situ measurements. *Appl. Opt.,* **34,** 6959–6975.

Borys, R. D., and M. A. Wetzel, 1997: Storm Peak Laboratory: A research, teaching, and service facility for the atmospheric sciences. *Bull. Amer. Meteor. Soc.,* **78,** 2115–2123.

Cahalan, R. F., W. Ridgeway, W. J. Wiscombe, T. L. Bell, and J. B. Snider, 1994: The albedo of fractal stratocumulus clouds. *J. Atmos. Sci.,* **51,** 2434–2455.

Chen, H., C. Y. She, P. Searcy, and E. Korevaar, 1993: Sodium-vapor dispersive Faraday Filter. *Opt. Lett.,* **18,** 1019–1021.

Davis, A. B., and A. Marshak, 2002: Space–time characteristics of light transmitted through dense clouds: A Green's function analysis. *J. Atmos. Sci.,* **59,** 2713–2727.

——, R. F. Cahalan, J. D. Spinhirne, M. J. McGill, and S. P. Love, 1999a: Off-beam lidar: An emerging technique in cloud remote sensing based on radiative green-function theory in the diffusion domain. *Phys. Chem. Earth,* **24B,** 177–185.

——, A. Marshak, H. Gerber, and W. J. Wiscombe, 1999b: Horizontal structure of marine boundary layer clouds from centimeter to kilometer scales. *J. Geophys. Res.,* **104,** (D6), 6123–6144.

Donovan, D. P., and A. C. A. P. van Lammeren, 2001: Cloud effective particle size and water content profile retrievals using combined lidar and radar observations. 1. Theory and examples. *J. Geophys. Res.,* **106,** 27 425–27 448.

Fox, N. I., and A. J. Illingworth, 1997: The retrieval of stratocumulus cloud properties by ground-based cloud radar. *J. Appl. Meteor.,* **36,** 485–492.

Gerber, H., Y. Takano, T. J. Garrett, and P. V. Hobbs, 2000: Nephelometer measurements of the asymmetry parameter, volume extinction coefficient, and backscatter ratio in Arctic clouds. *J. Atmos. Sci.,* **57,** 3021–3034.

King, M. D., 1986: Multiwavelength scanning radiometer from airborne measurements of scattered radiation within clouds. *J. Atmos. Oceanic Technol.,* **3,** 513–522.

Knollenberg, R. G., 1981: Techniques for probing cloud microstructure. *Clouds, Their Formation, Optical Properties, and Effects,* P. V. Hobbs and A. Deepak, Eds., Academic Press, 15–91.

Korolev, A. V., G. A. Isaac, J. W. Strapp, and A. N. Nevzorov, 1999: In situ measurements of effective diameter and effective droplet number concentration. *J. Geophys. Res.,* **104,** 3993–4003.

Koshak, W. J., R. J. Solakiewicz, D. D. Phanord, and R. J. Blakeslee, 1994: Diffusion model for lightning radiative transfer. *J. Geophys. Res.,* **99,** 14 361–14 371.

Liao, L., and K. Sassen, 1994: Investigation of relationships between Ka-band radar reflectivity and ice and liquid water contents. *Atmos. Res.,* **34,** 231–248.

Love, S. P., A. B. Davis, C. Ho, and C. A. Rohde, 2001: Remote sensing of cloud thickness and liquid water content with Wide-Angle Imaging Lidar (WAIL). *Atmos. Res.,* **59–60,** 295–312.

Nakajima, T., and M. D. King, 1990: Determination of the optical thickness and effective particle radius of clouds from reflected solar radiation measurements. Part I. Theory. *J. Atmos. Sci.,* **47,** 1878–1892.

Pilewskie, P., and S. Twomey, 1987: Discrimination of ice from water in clouds by optical remote sensing. *Atmos. Res.,* **21,** 113–122.

Platnick, S., 2000: Vertical photon transport in cloud remote sensing problems. *J. Geophys. Res.,* **105,** 22 919–22 935.

Schertzer, D., and S. Lovejoy, 1987: Physical modeling and analysis of rain and clouds by anisotropic scaling multiplicative processes. *J. Geophys. Res.,* **92,** 9693–9714.

Twomey, S., and T. Cocks, 1982: Spectral reflectance of clouds in the near-infrared: Comparison of measurements and calculations. *J. Meteor. Soc. Japan,* **60,** 583–592.

Varnai, T., and A. Marshak, 2001: Statistical analysis of the uncertainties in cloud optical depth retrievals caused by three-dimensional radiative effects. *J. Atmos. Sci.,* **58,** 1540–1548.

Zmarzly, P. M., and R. P. Lawson, 2000: An optical extinctometer for cloud radiation measurements and planetary exploration. Final report submitted to NASA Goddard Space Flight Center in fulfillment of Contract NAS5-98032, 131 pp.